

High-fidelity simulations of the lobe-and-cleft structures and the deposition map in particle-driven gravity currents

L. F. R. Espath, L. C. Pinto, S. Laizet, and J. H. Silvestrini

Citation: [Physics of Fluids \(1994-present\)](#) **27**, 056604 (2015); doi: 10.1063/1.4921191

View online: <http://dx.doi.org/10.1063/1.4921191>

View Table of Contents: <http://scitation.aip.org/content/aip/journal/pof2/27/5?ver=pdfcov>

Published by the [AIP Publishing](#)

Articles you may be interested in

[Assessment of the role of axial vorticity in the formation of particle accumulation structures in supercritical Marangoni and hybrid thermocapillary-rotation-driven flows](#)

Phys. Fluids **25**, 012101 (2013); 10.1063/1.4769754

[Decaying versus stationary turbulence in particle-laden isotropic turbulence: Turbulence modulation mechanism](#)

Phys. Fluids **24**, 015106 (2012); 10.1063/1.3678332

[Gravity-driven slug motion in capillary tubes](#)

Phys. Fluids **21**, 052003 (2009); 10.1063/1.3125262

[Plane Poiseuille flow of a sedimenting suspension of Brownian hard-sphere particles: Hydrodynamic stability and direct numerical simulations](#)

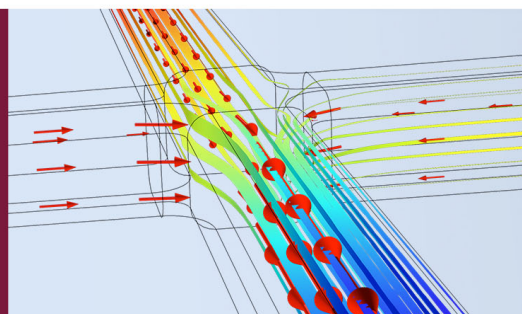
Phys. Fluids **18**, 054103 (2006); 10.1063/1.2199493

[Mechanisms for deposition and resuspension of heavy particles in turbulent flow over wavy interfaces](#)

Phys. Fluids **18**, 025102 (2006); 10.1063/1.2166453

How to Simulate &
Design Microfluidics
Devices

 COMSOL



High-fidelity simulations of the lobe-and-cleft structures and the deposition map in particle-driven gravity currents

L. F. R. Espath,¹ L. C. Pinto,¹ S. Laizet,^{2,a)} and J. H. Silvestrini¹

¹*Faculdade de Engenharia, Pontifícia Universidade Católica do Rio Grande do Sul, Ave. Ipiranga 6681, 90619-900 Porto Alegre-RS, Brasil*

²*Turbulence, Mixing and Flow Control Group, Department of Aeronautics, Imperial College London, London SW7 2AZ, United Kingdom*

(Received 22 December 2014; accepted 4 May 2015; published online 18 May 2015)

The evolution of a mono-disperse gravity current in the lock-exchange configuration is investigated by means of direct numerical simulations for various Reynolds numbers and settling velocities for the deposition. We limit our investigations to gravity currents over a flat bed in which density differences are small enough for the Boussinesq approximation to be valid. The concentration of particles is described in an Eulerian fashion by using a transport equation combined with the incompressible Navier-Stokes equations. The most interesting results can be summarized as follows: (i) the settling velocity is affecting the streamwise vortices at the head of the current with a substantial reduction of their size when the settling velocity is increased; (ii) when the Reynolds number is increased the lobe-and-cleft structures are merging more frequently and earlier in time, suggesting a strong Reynolds number dependence for the spatio-temporal evolution of the head of the current; (iii) the temporal imprint of the lobe-and-cleft structures can be recovered from the deposition map, suggesting that the deposition pattern is defined purely and exclusively by the structures at the front of the current. © 2015 AIP Publishing LLC. [<http://dx.doi.org/10.1063/1.4921191>]

I. INTRODUCTION

Turbidity currents are gravity-driven underflows, where the driving density difference is caused by particles in suspension.^{1,2} The particle concentration may be enhanced by erosion at the bed and reduced by deposition. They exhibit complex dynamics, with lobe-and-cleft instabilities forming at the front followed by a region of intense mixing through spanwise Kelvin-Helmholtz-type billows forming at the interface between the current and the ambient fluid.³

Turbidity currents are an important mechanism in nature and they play a crucial role in geological events with, for instance, the formation of topographical features such as channels, gullies, sediment waves, and levees.^{4–8} They can develop when the fresh water of a river meets the salt water of the ocean with the ability to change the physical shape of the sea floor by eroding large areas and/or by depositing large amounts of sediment. They can also have a central role in the formation of hydrocarbon reservoirs^{1,9} and they can impact the stability of submarine structures placed at the sea-floor like pipelines or submarine's cables.^{10,11}

It is clear that understanding the physical mechanism associated with these currents as well as the correct prediction of their main features is of great importance for practical and theoretical purposes. One of the key features of turbidity currents is the lobe-and-cleft structures located at the head of the current. There has been an intensive effort to study those structures, with many experimental investigations,^{3,7,12–15} theoretical approaches,^{16,17} and more recently with numerical investigations based on Direct Numerical Simulations (DNS).^{18–24} Experiments^{3,7,12} investigating

^{a)}s.laizet@imperial.ac.uk

lobe-and-cleft patterns have typically imaged the gravity current from below, allowing the growth, merging, and bifurcation of the structures to be tracked. This analysis identified the origin of the instability as the unstable stratification generated as ambient fluid is overrun by the current head, subject to a frictional surface. As a convincing argument, further experiments have been successfully carried out using a moving floor in the direction of the current in order to suppress this instability.^{7,12} However, a more recent study¹⁴ has shown that as the gravity current propagates, the lobe-and-cleft structures are less sensitive to the gravitational instability, suggesting the existence of an alternative Reynolds number-dependent mechanism creating the instability generating lobe-and-cleft patterns.

Several numerical studies also focus on the lobe-and-cleft structures in the lock-exchange configuration over flat beds^{18–21,25,26} but also with slightly more complex bed topography.^{23,27} They provide detailed and valuable information about the dynamics of turbidity currents with, for instance, the spatio-temporal evolution of the energy budgets, particle concentration field, or wall shear stress. Unfortunately, only very few DNS were carried out with a relatively high Reynolds number and with particle sedimentation. For turbidity currents with sedimentation, the highest Reynolds number simulated to date is 10 000 (Reynolds number defined with the half-size h of the vertical computational domain as a reference length).²² Comparisons between 2D and 3D simulations for various Reynolds numbers were used to assess which quantities of interest for the geoscientist could be evaluated quickly with a 2D simulation. It was found that a 2D simulation is not able to predict accurately the main features obtained in a 3D simulation, with maybe the exception of the sedimentation rate for which a qualitative agreement can be found between the 2D and the 3D simulations. The highest Reynolds number reached by DNS for a planar density-driven gravity current is 7500 (15 000 if the Reynolds number is defined using the total height $2h$ of the computational domain).²⁶ The objective of the authors was to identify, visualize, and describe the turbulent structures and their influence on the flow dynamics. The authors found that the near-wall bottom flow can be very similar to a turbulent boundary layer flow with several longitudinal hairpin like structures and preferential patterns of low and high speed streaks. They also noticed that most of the erosive power of the flow is found in the gravity current front. However, the sedimentation was not taken into account in those simulations. For 2D simulations, the highest Reynolds number reached was 30 000 for a linear-stability analysis of a 2D gravity-current front.^{18,19} The analysis was undertaken in order to clarify the instability mechanism that leads to the formation of the complex lobe-and-cleft structures. A good agreement was found between the 2D linear-stability analysis and a low Reynolds number 3D DNS only for the early stage of the spatial development of the current.

In the present numerical investigation, the main aim is to better understand how the particle settling velocity affects the spatio-temporal evolution of a gravity current, in particular the lobe-and-cleft structures at the front, for various Reynolds numbers. A strong connection is made between the deposition map and the imprint of the lobe-and-cleft structures. After briefly describing the problem configuration and the numerical strategy, we start our investigations by presenting the main features of the flow with 3D visualizations and with the temporal evolution of the front location, sedimentation rate, and suspended particle mass, followed by the temporal evolution of the full energy budget. Finally, we try to link the structures at the head of the current with the deposition patterns at the bottom of the channel before ending with a conclusion section.

II. PROBLEM CONFIGURATION AND GOVERNING EQUATIONS

In this paper, we focus on the prediction of a mono-disperse dilute suspension particle-laden flow in the typical lock-exchange configuration over a flat bed. Uniformly suspended sediment particles are enclosed in a small portion $L_{1b} \times L_{2b} \times L_{3b}$ of the computational domain $L_1 \times L_2 \times L_3$ separated by a gate with the ambient fluid. The flow configuration is shown in Figure 1 and is exactly the same as in our previous work.²² We assume a small volume fraction of the particles (typically less than 1%) so that interactions among the particles, such as hindered settling and/or particle inertia can be neglected. The coupling between particle and fluid motion is dominated by the transfer of momentum, rather than volumetric displacement effects. The particles are assumed

TABLE I. Summary of numerical parameters.

Re	L_1, L_2, L_3	n_1, n_2, n_3	Δt	u_s
2 236	18, 2, 2	1441, 221, 201	6.024×10^{-4}	0
2 236	18, 2, 2	1441, 221, 201	6.024×10^{-4}	0.02
2 236	18, 2, 2	1441, 221, 201	6.024×10^{-4}	0.03
2 236	18, 2, 2	1441, 221, 201	6.024×10^{-4}	0.04
5 000	18, 2, 2	1537, 257, 257	5×10^{-4}	0.02
10 000	18, 2, 2	2305, 513, 385	3×10^{-4}	0.02

III. NUMERICAL METHODS AND PARAMETERS

The simulations are performed with the high-order flow solver **Incompact3d** which is based on sixth-order compact schemes for spatial discretization on a Cartesian mesh and a third-order Adams-Bashforth scheme for time advancement. To treat the incompressibility condition, a fractional step method requires to solve a Poisson equation. The main originality of this code is that this equation is fully solved in spectral space via the use of relevant 3D Fast Fourier transforms (FFTs), which allows the use of different boundary conditions in each spatial direction. Using the concept of the modified wavenumber,³² the divergence free condition is ensured up to machine accuracy. The pressure mesh is staggered from the velocity one by half a mesh to avoid spurious pressure oscillations. More details about the present code and its validation can be found in Ref. 33. For this numerical work, the version of **Incompact3d** based on a scalable 2D domain decomposition is used in order to run the simulations on parallel supercomputers. See Ref. 34 for a detailed description of the domain decomposition strategy.

The parameters of the six 3D simulations are presented in Table I. Three different Reynolds numbers are simulated with a settling velocity of 0.02. For the lowest Reynolds number, three extra simulations are performed: a reference simulation with no settling velocity and two simulations with settling velocities equal to 0.03 and 0.04. When expressed as dimensional quantities, the particle diameter is between $19.94 \mu\text{m}$ and $42.18 \mu\text{m}$ and the settling velocities are of the order of 0.005 m/s for a channel height of 0.125 m, corresponding to middle to coarse silt particles. The Schmidt number is fixed to $Sc = 1$ for all the simulations. We consider a subdomain of $(L_{1b}, L_{2b}, L_{3b}) = (1, 2, 2)$ to define the box containing the particle-fluid mixture. All the simulations are performed for a non-dimensional time of $t = 60$ except for the simulation with $Re = 10\,000$ which is stopped at $t = 32$ for computational constraints. The perturbation added onto the initial velocity field is adjusted in order to get an initial kinetic energy equal to $\approx 1\%$ of the initial potential energy.

The numbers of mesh nodes and the size of the simulations have been carefully chosen in order to solve the smallest scales of the flow. In a previous paper,²² we successfully compared our simulations with previous numerical data²⁰ and experimental data.³⁵

IV. GENERAL FEATURES OF THE FLOW

The sudden release of the particle-fluid mixture along the left wall of the computational domain leads to the streamwise evolution of a gravity current into the ambient fluid. At the very early stage of the simulation, before $t = 8$, the motion is mainly two dimensional for the low Reynolds number case whereas it already has some 3D features for the highest Reynolds number case.²² At $t = 8$, three-dimensional structures can be observed in the six simulations as shown in Figure 2. The gravity current can be separated into two parts: the head of the current, still transitioning toward a turbulence state where the lobe-and-cleft patterns can be observed, and the core of the current, with 3D turbulent features and a wider range of scales when the Reynolds number is increased. It seems also that at $t = 8$ the settling velocity is not influencing the flow too deeply, at least based on the Q -criterion. The only noticeable difference is maybe an attenuation of the turbulent activity at the head of the current when the settling velocity is increased. At $t = 20$, it can be seen that the head

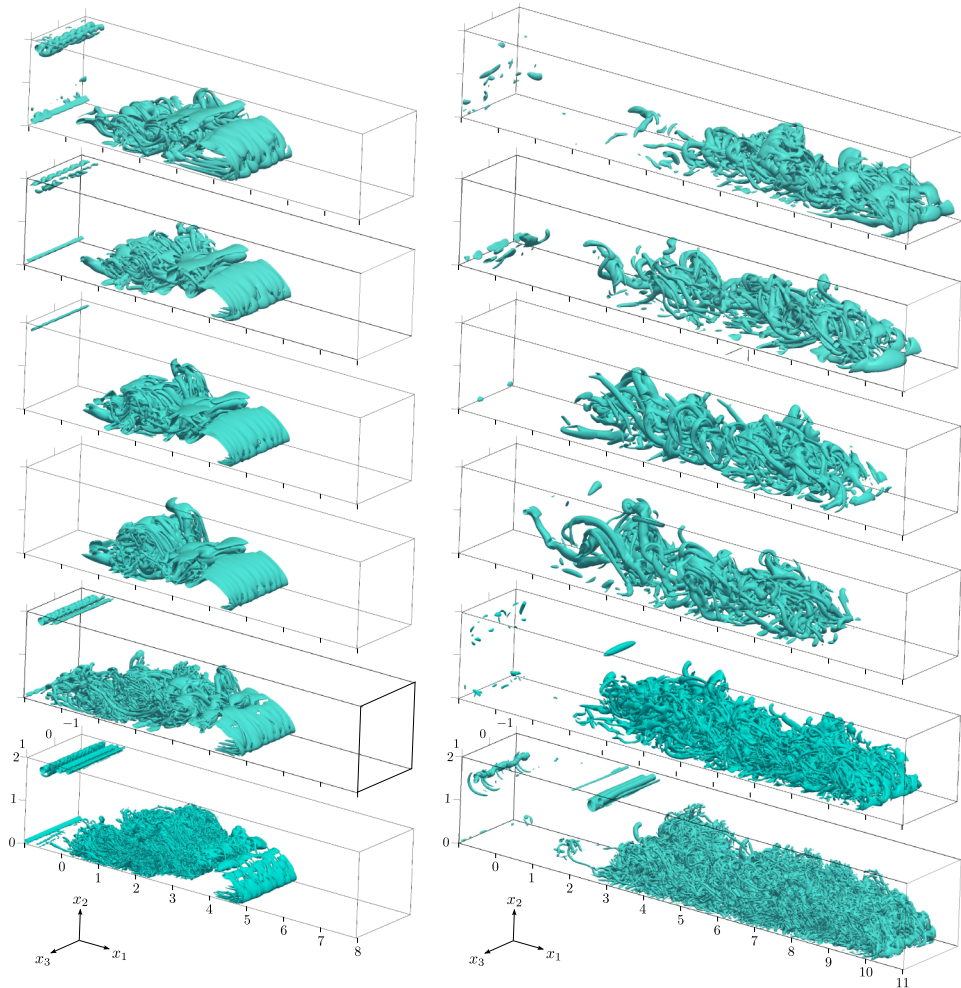


FIG. 2. Turbulent structure of the gravity currents illustrated by the Q -criterion for the isovalue $Q = 1$ with (from top to bottom): $Re = 2236$ with $u_s = 0, 0.02, 0.03, 0.04$; $Re = 5000$ and $Re = 10000$ both with $u_s = 0.02$ at $t = 8$ (left) and $t = 20$ (right).

and the tail of the current are both fully turbulent with very intense vortices, mainly orientated in the streamwise direction. When the Reynolds number is increased, more and more structures of smaller and smaller size can be observed in the core of the current. Finally, when the settling velocity is increased, it seems that the head of the current is slowing down as the structures highlighted in Figure 2 are further away from the end of the visualization box located at $x_1 = 11$.

Snapshots of the concentration field are shown in Figure 3 at $t = 8$ and $t = 20$ for $x_3 = 0$ corresponding to the middle-plane of the computational domain in the spanwise direction. It is possible to see that the tail and the top of the current are exhibiting more turbulent features when the Reynolds number is increased, leading to an acceleration of the deposition process. Interestingly, when the settling velocity is increased, the tail of the current is different, with very intense values for the concentration field above 0.3 when $u_s = 0.04$ whereas only values up to about 0.15 can be observed when $u_s = 0.02$. For the reference case with no deposition, it is very difficult to identify clearly Kelvin-Helmholtz vortices at the tail of the current. Instead, very intense values in a very homogeneous concentration field can be observed. At $t = 20$, almost all the particles have deposited for the simulation with the highest settling velocity. Finally, the concentration field at the interface exhibits more complex and finest features when the Reynolds number is increased.

Figure 4 shows the profiles of the streamwise velocity at $t = 8$ and $t = 20$ after an average in the spanwise direction. At $t = 8$, the highest values for the streamwise velocity are located in the

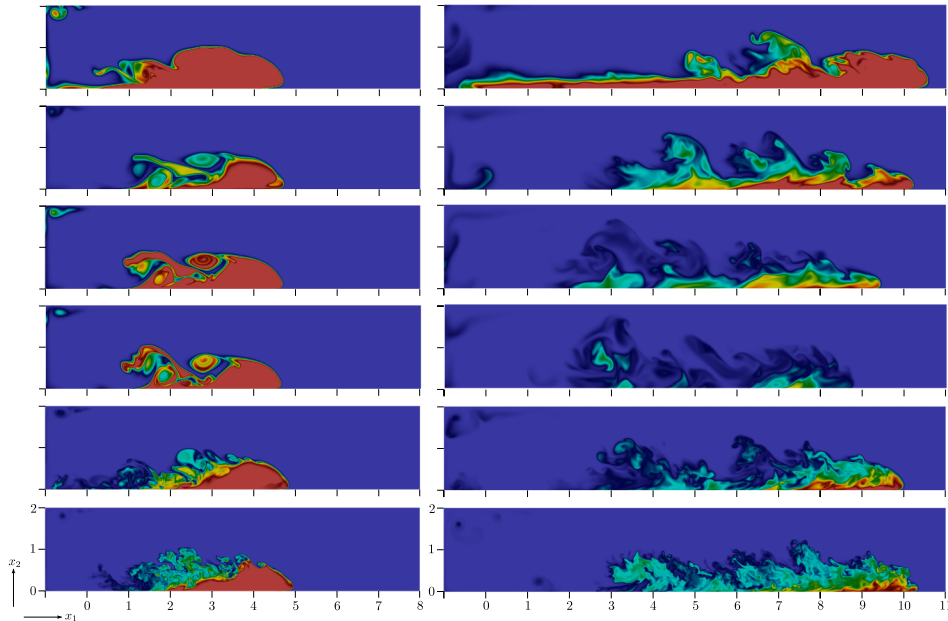


FIG. 3. Concentration field (the color red corresponds to $c > 0.3$, the color blue to $c = 0$) for $x_3 = 0$, (left) $t = 8$, (right) $t = 20$ (from top to bottom $Re = 2236$ with $u_s = 0, 0.02, 0.03, 0.04$, $Re = 5000, 10000$ both with $u_s = 0.02$).

core of the current (location $x_1 = 2$). It suggests that the structures at the top of the current, the Kelvin-Helmholtz vortices, are eventually convected slightly faster than the lobe-and-cleft structures. Interesting features at $x_1 = 2$ and $x_1 = 3$ are the negative values for the streamwise velocity very close to the wall for $x_2 < 0.05$. This trend is more pronounced for the lowest Reynolds number and for the highest settling velocity. As a result, there is a separation region for a short period of time that could be induced by a Kelvin-Helmholtz vortex as suggested by Figure 3. Finally, for $x_1 = 5$, corresponding to the head of the flow, only the Reynolds number is affecting the velocity profiles close to the wall for $x_2 < 0.25$, with an acceleration of the flow when the Reynolds is increased. At $t = 20$, as the current is fully turbulent, we can observe more conventional boundary layer profiles for the streamwise velocity, even in the core of the current, for $0 < x_2 < 0.9$. However, considering the Reynolds numbers in this numerical work, it is clear that the velocity profiles presented here do not fit with a log law scaling. Even though, the flow exhibits some features highlighted in previous numerical studies²⁶ such as longitudinal hairpin like structures and preferential patterns of low and high speed streaks. Because they are travelling slower than the Kelvin-Helmholtz vortices at the early stages of the simulations, the lobe-and-cleft structures at the bottom of the computational domain eventually interact with the Kelvin-Helmholtz vortices, giving rise to a fully turbulent gravity current. This figure also confirms that when the settling velocity is increased, the head of the current is

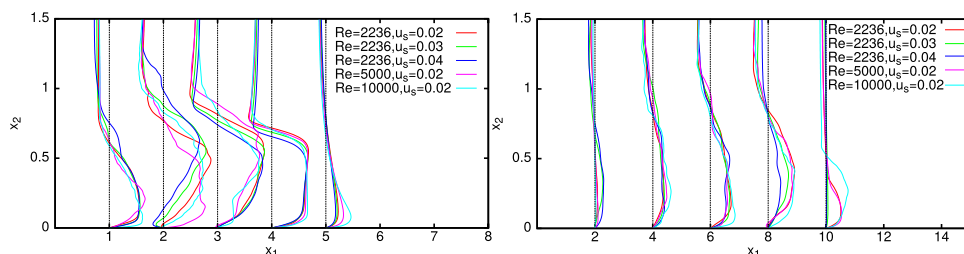


FIG. 4. Profiles for different streamwise locations of the streamwise velocity at $t = 8$ (left) and $t = 20$ (right) after an average in the spanwise direction.

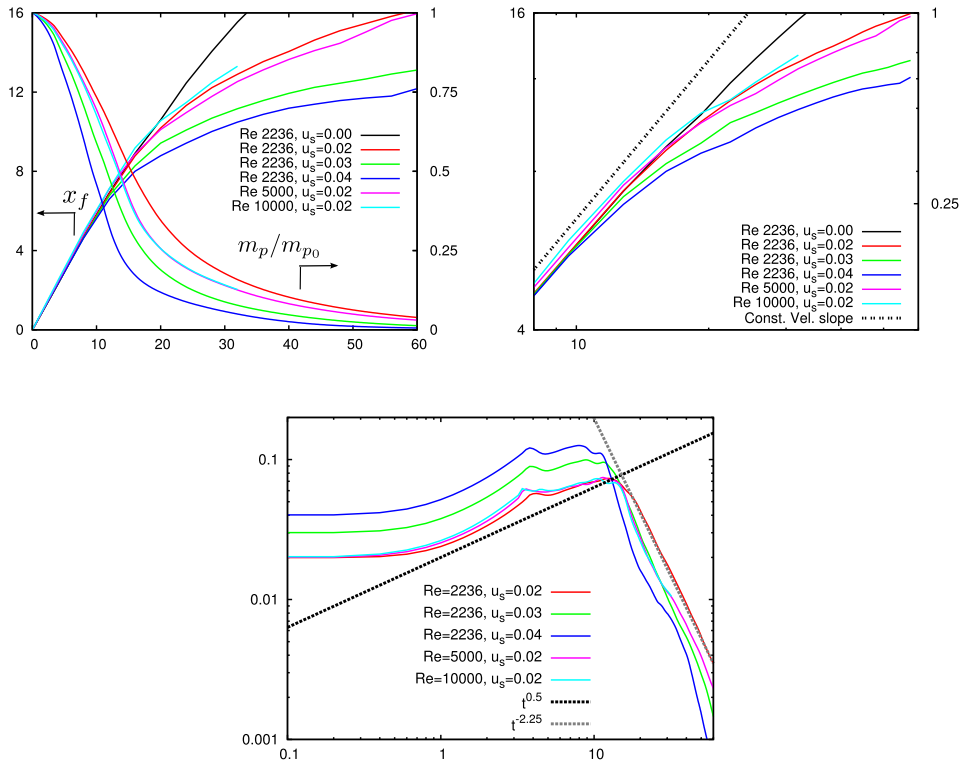


FIG. 5. Time evolution of the front location $x_f(t)$ and suspended particle mass $m_p/m_{p0}(t)$ (top, left), the front location using logarithmic scales (top right) and the sedimentation rate $\dot{m}_s(t)$ (bottom).

evolving slower. We can see that at $t = 20$ for $u_s = 0.04$, the streamwise velocity profile is almost zero at $x_1 = 10$, suggesting that the current has not reached yet this streamwise location.

The temporal evolution of the front location $x_f(t)$, the suspended particle mass $m_p/m_{p0}(t)$, and the sedimentation rate $\dot{m}_s(t)$ are shown in Figure 5. The front location x_f corresponds to the first streamwise location where the streamwise component of the concentration gradient (after an average in the spanwise direction) is non-zero when starting from the end of the computational domain. The suspended particle mass normalized by the initial suspended mass m_p/m_{p0} is defined as $m_p(t) = \int_{\Omega} c dV$ while the sedimentation rate $\dot{m}_s(t)$ is defined as $\dot{m}_s = \frac{1}{L_1 L_3} \int_0^{L_1} \int_0^{L_3} c_w(x_1, x_3, t) u_s dx_3 dx_1$, where c_w is the concentration at the wall. The temporal evolution of the front location $x_f(t)$ in Figure 5 shows that the front velocity deviates quite quickly (after $t = 10$) from a straight line (observed when there is no settling velocity), with a substantial decrease due to the deposition. The deviation is obviously more and more pronounced when the settling velocity is increased. A variation of the Reynolds number has a limited impact for x_f . For all the simulations, after a brief initial period of acceleration, a fairly large period of near constant velocity is obtained, in agreement with previous studies.²⁵ To summarize, it is possible to identify an initial phase where the velocity sharply increases, a phase where the velocity is nearly constant, and a final phase where the front velocity decays because of the particle deposition. Concerning the suspended mass $m_p/m_{p0}(t)$, the value obtained at the end of the simulation is lower than 5% for all cases but a much faster decay can be observed when the settling velocity is increased. It seems also that for high Reynolds numbers ($Re = 5000, 10000$), the evolution of the suspended mass is nearly the same.

Concerning the sedimentation rate, the initial values for $\dot{m}_s(t) = 0.02, 0.03$, or 0.04 correspond to the settling velocities. The sedimentation rate is slowly increasing for all cases up to $t \approx 10$ with different values but with a similar evolution at the same slow rate of about $t^{0.5}$, in agreement with the numerical data of Ref. 20. At the early stage of the simulations, there is very little mixing between the suspended particles and the ambient fluid. Turbulent motions are only developing at the tail of the current and they would not have reached yet the head of the current, as shown in Figure 2 for

$t = 8$. A peak value is reached for $11 < t < 15$, with a very weak Reynolds number dependence and a rather significant dependence with the settling velocity. After the peak, the sedimentation rate suddenly decreases very quickly at a rate of about $t^{-2.5}$. After $t \approx 15$, the current is fully turbulent from its head to its tail with intense turbulent motions everywhere. One can expect the sedimentation rate to be larger than the one for a current with less turbulent features, for which mixing is less likely to happen. We will see in the following that the sedimentation process is strongly related to the structures at the head of the current and to its turbulence activity. The more turbulence close to the bottom of the channel the more mixing in the current, with a larger number of particles more likely to deposit.

V. ENERGY BUDGETS

In this section, we investigate how the temporal evolution of the different energy components is affected by the streamwise growth of the current. In particular, we focus on the influence of the settling velocity as we already discussed the influence of the Reynolds number in a previous study²² where the framework of the analysis of the energy budget is explained in great detail. The rate of change for the total energy is given by

$$\begin{aligned} \frac{d(k + E_p)}{dt} &= - \int_{\Omega} \frac{2}{Re} \mathbf{s} : \mathbf{s} d\Omega + \int_{\Omega} \left(\frac{1}{ScRe} x_2 \nabla^2 c + x_2 u_s \frac{\partial c}{\partial x_2} \right) d\Omega \\ &= -\epsilon - \epsilon_s, \end{aligned} \quad (3)$$

where ϵ is associated to the turbulent dissipation (macro-dissipation at macroscopic scale) while ϵ_s is the dissipation associated with loss of energy due to suspended particles (micro-dissipation at microscopic scale). $k(t) = \int_{\Omega} \frac{1}{2} \mathbf{u} \cdot \mathbf{u} d\Omega$ and $E_p(t) = \int_{\Omega} c x_2 d\Omega$ are the kinetic and potential energy components, respectively. In order to study the temporal evolution of ϵ and ϵ_s , we define E_d and E_s as the time integrals of the dissipation components ϵ and ϵ_s with

$$E_d(t) = \int_0^t \epsilon(\tau) d\tau \quad \text{and} \quad E_s(t) = \int_0^t \epsilon_s(\tau) d\tau. \quad (4)$$

Integrating Eq. (3) in time yields to the following equation:

$$k + E_p + E_d + E_s = E_T = E_{T_0} = cst, \quad (5)$$

where E_{T_0} is the energy available in the computational domain at the beginning of the simulation. Note that in our approach, we consider the full budget equation for the kinetic energy. A similar approach, with simplifying assumptions, can be found in Ref. 21. The main difference between the present work and the work of Ref. 21 is that we compute the exact energy equation without any assumptions over the dissipation terms.

Figure 6 presents the temporal evolution of the energy budget with the time history of all energy components for the 4 simulations with $Re = 2236$. The data presented are normalized with E_{T_0} which is the total energy of the system at $t = 0$. The first important result here is that E_T is constant in our simulations, meaning that the energy is well conserved. At the very early stage of the simulations (before $t = 5$), there is a rapid conversion of potential energy into kinetic energy which has a peak at $t \approx 4$ followed by a steady decay. This decay is caused by the increasing influence of the dissipation which is playing a key role along the development of the current. At the end of the simulation, the kinetic energy and the potential energy are virtually close to zero. A very interesting result is that at the early stage of the temporal evolution of the current, the settling velocity is strongly affecting the evolution of the micro-dissipation. For instance, the micro-dissipation is more important than the macro-dissipation for up to $t = 10$ for the simulation with $u_s = 0.03$ and for up to $t = 15$ for the simulation with $u_s = 0.04$, corresponding to the time when the head of the current becomes fully turbulent. After $t \approx 15$, this trend is inverted and by the final time of the simulation, the macro-dissipation E_d accounts for about 55% – 60% of dissipation of the initial potential energy. At the end of the simulation, $E_d \approx 55\%$ and $E_s \approx 42\%$ for $u_s = 0.04$ whereas $E_d \approx 60\%$ and $E_s \approx 22\%$ for $u_s = 0.02$. Sedimentation accounts for a substantial loss of energy which is hence not

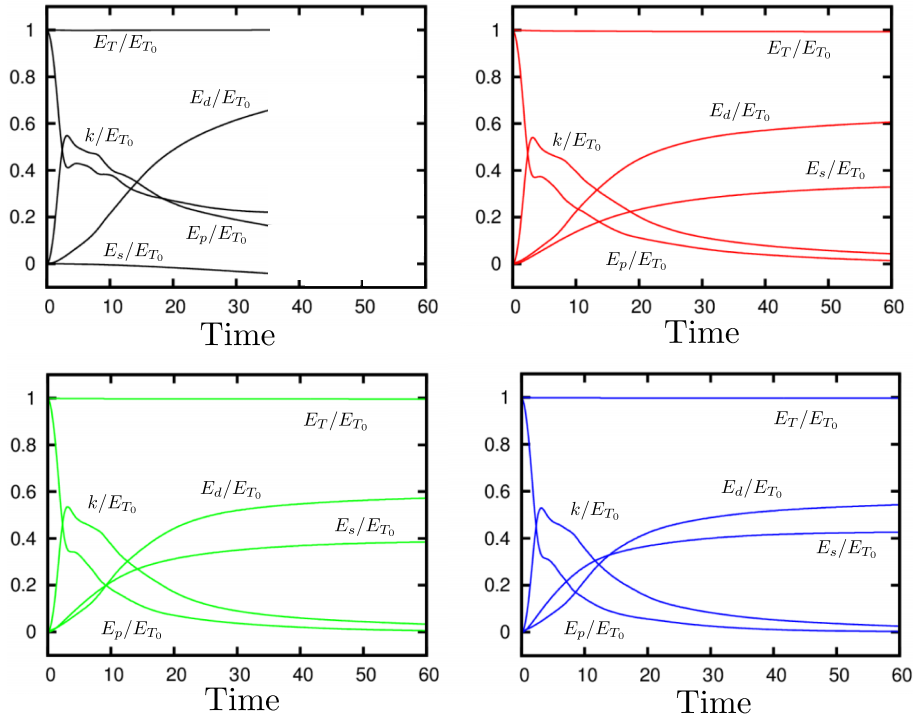


FIG. 6. Time history of the kinetic and potential energy, turbulent and particle-settling dissipation for the 4 simulations with $Re = 2236$. Top left: $u_s = 0$; Top right: $u_s = 0.02$; Bottom left: $u_s = 0.03$; Bottom right $u_s = 0.04$.

available for transport and mixing. Furthermore, there is a strong correlation between the level of energy dissipated by sedimentation and the settling velocity: more energy is lost by sedimentation when the settling velocity is increased. As already discussed in our previous study,²² the influence of the Reynolds number on the temporal evolution of the energy budget is quite weak, except maybe for the peak of kinetic energy that is slightly increased when the Reynolds number is increased. The simulation with a non-zero settling velocity confirms that the macro-dissipation E_d is strongly affected by the settling velocity with a high value of nearly 80% obtained at $t = 60$. Furthermore, because the head of the current is reaching the end of the computational domain at about $t = 35$, we do not plot the curves after $t = 35$. It is another evidence that the sedimentation is clearly slowing down the current. Finally, it is important to point out that the micro-dissipation is negative as the term relative to the settling velocity is zero and cannot balance the negative Laplacian term (see Eq. (3)).

VI. FRONT STRUCTURES AND DEPOSITION PATTERNS AT THE WALL

In this section, we focus on the characteristics of the head of the current structures, namely, the lobe-and-cleft patterns, and their relation with the 2D deposition at the wall expressed as

$$D_r(x_1, x_3, t) = \int_0^t c_w(x_1, x_3, \tau) u_s d\tau. \quad (6)$$

At $t = 8$, the structure at the front can be analyzed in detail through visualizations of the concentration field as shown on the left side in Figure 7 for $c = 0.25$. A cross section of the Q -criterion for the selected vertical planes upstream of the front is shown at the right side of the same picture. The lobe-and-cleft patterns can be well identified with regions between two streamwise vortices (indicated in red with positive values of Q -criterion), the lobes, along with regions with an important deformation rate, the clefts. As suggested in Figure 7, the spatial organisation of the lobe-and-cleft structures is far more complex when the Reynolds number is equal to 10000, with

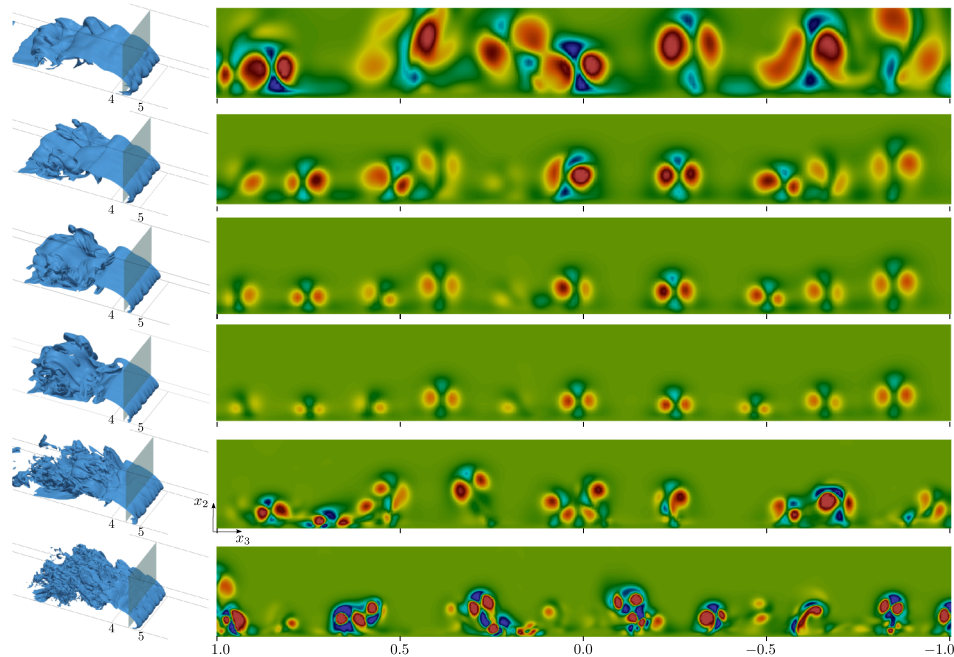


FIG. 7. Structure of the front by isosurface for $c = 0.25$ (left) and Q -criterion with isovalues ranging from $-25 < Q < 25$ (right) at $t = 8$. The plane is located at a distance of $0.33h$ behind the head of the current. From top to bottom: $Re = 2236$ with $u_s = 0, 0.02, 0.03, 0.04$; $Re = 5000$ and $10\,000$ with $u_s = 0.02$. Red indicates $Q > 0$ and blue $Q < 0$.

regions of high deformation rate and high vorticity on top of each other. This can be explained by a faster transition into a turbulent state for the head of the front when the Reynolds number is increased. Furthermore, when the Reynolds number is increased, the lobe-and-cleft structures are more intense suggesting a stronger turbulence activity at the head of the current. For the reference simulation with no deposition, the lobe-and-cleft structures are much larger and more intense by comparison to the ones observed when the deposition is present since no micro-dissipation is expected for this conservative current. When the settling velocity is increased, the lobe-and-cleft structures are getting smaller and smaller and are less intense. Quite remarkably, the location of most of those structures in the spanwise direction is not changing, highlighting the deterministic character of our simulations (same random noise at the gate for all the simulations). Finally, it is important to note that because of the strong influence of the settling velocity, comparisons with previous numerical work where the deposition was not taken into account^{26,27} are not relevant.

The authors in Refs. 3, 7, and 12 showed experimentally that the lobe-and-cleft structures at the front arise from a gravity instability produced by the ambient fluid which is overrun by the particle concentration of the gravity current. The front structure can be seen in great detail in Figure 8 with visualizations in the (x_1, x_2) (side view) and (x_1, x_3) (bottom view) planes of the Q -criterion with an isovalue of 1. For this figure, the longitudinal black lines, obtained from the deposit map, correspond to the signature of the clefts. At $t = 8$, the front is well defined, with very long streamwise vortices at the bottom surface. When the Reynolds number is increased, the lobes and the clefts are getting thinner and thinner and therefore their spanwise wavelength is expected to be larger. At $t = 14$, the structures are more complex, with a shorter length in the streamwise direction, especially for the low Reynolds number cases. Highly complex structures at the head of the current can be observed with lobes of different sizes nested into each other. Some lobes have merged together, a phenomenon already reported experimentally by Refs. 7 and 14 and clearly visible for the simulations with $Re = 10\,000$ when looking at the temporal map of the front structure's signature. A merging is highlighted in Figure 9. At $t = 6$, we can see three tooth like structures at the head of the front. The structure in the middle is then progressively split in two parts, each of them merging with the neighboring structures. As a result, at $t = 9$ two larger tooth like structures can be observed.

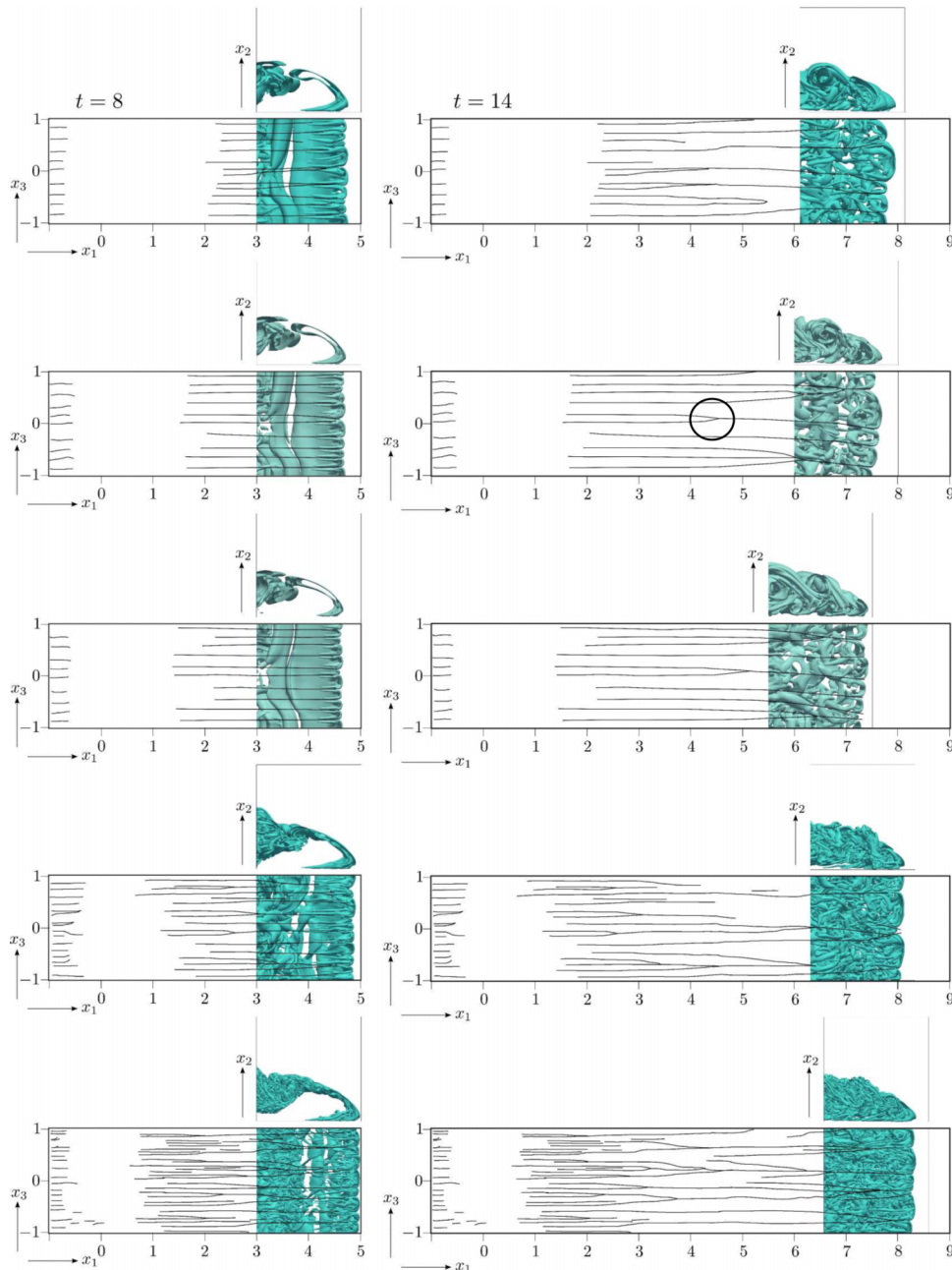


FIG. 8. Visualization in the (x_1, x_2) and (x_1, x_3) planes of the front structures along with their signatures by plotting the Q-criterion with an isovalue equal to 1, for $t = 8$ (left) and $t = 14$ (right). From top to bottom: $Re = 2236$ with $u_s = 0.04, 0.03, 0.02$; $Re = 5000$ and $10\,000$ with $u_s = 0.02$. The black circle corresponds to the merging in Figure 9.

The signature of the front structures is presented in Figure 10 at $t = 30$ for the simulations with $Re = 2236$ and $u_s = 0.02$ and with $Re = 10\,000$ and $u_s = 0.02$. When $Re = 10\,000$, a new instability is developing at the front of the current with fish bone skeleton structures visible on the temporal signature of the structures. It seems that there is a critical spanwise size for the lobes of about $0.5h$ for $Re = 10\,000$. When the lobes reach this critical size, a local instability causes the lobes to crack, similarly to what happens to the ice at the head of a glacier. This local instability, which is not strong enough to provoke a complete break-up of a lobe, could be triggered by the increasing number of very intense thin structures localized within each lobe as shown in Figure 8. Further investigations

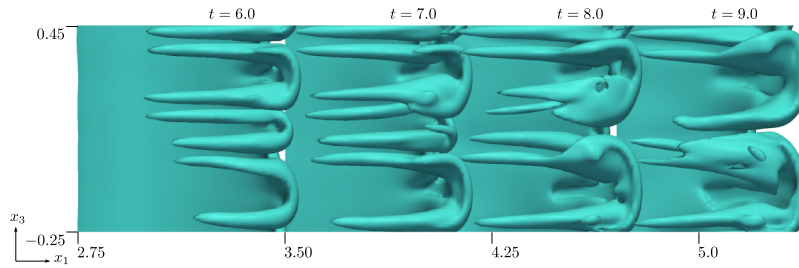


FIG. 9. Visualization of the merging process for the lobe-and-cleft patterns using the Q -criterion between $t = 6$ and $t = 9$ for the simulation with $Re = 2236$ and $u_s = 0.03$. This merging is highlighted in Figure 8 by a black circle.

are needed at this point to better characterize this new instability with DNS at higher Reynolds numbers and with a larger computational domain in the spanwise direction.

Using Figure 8, it is possible to carry out a quantitative analysis of the size of the lobe-and-cleft structures during the temporal evolution of the current. At $t = 8$, when the settling velocity is increased, the size of lobe-and-cleft structures is reduced from a spanwise average of about $0.3h$ for the simulation with a settling velocity of 0.02 to a spanwise average of about $0.2h$ for the simulation with a settling velocity of 0.04 . At this stage, the Reynolds number is not affecting the spanwise average size of the structures. At $t = 14$, the six simulations exhibit more or less the same spanwise average size of $0.4h$, similar to the sizes reported experimentally by Ref. 12 and numerically by Ref. 20. In the numerical work of Ref. 26, where the deposition is not taken into account, the spanwise average size is slightly larger than the ones reported in the present work with a value of about $0.5h$ for a Reynolds number of 7500 , however, consistent with Figure 7. At a more advanced stage of the development of the current, the spanwise average size can be larger than h in our low Reynolds number simulations, whereas because of the local instability there is a critical size of about $0.5h$ for our simulation with $Re = 10\,000$. A new simulation with a large spanwise domain would help to check the influence of the size of the computational domain on this critical spanwise size for the lobes.

A schematic representation of the lobe-and-cleft patterns is presented in Figure 11 in the (x_2, x_3) and (x_1, x_3) planes. This figure is a summary of Figures 7 and 8 with a frontal and a bottom wall view of the head of the current. The schematic characteristics of the lobe-and-cleft structures presented here are important with respect to the front formation, the distribution of strain rate ($\underline{\underline{s}}$) and rotation rate ($\underline{\underline{w}}$), and the relation between the spanwise wavelength of the front and the shape of the deposition. We can identify a cleft structure as a region of high strain rate ($Q < 0$, corresponding to $\underline{\underline{s}} > \underline{\underline{w}}$ in Figure 11). It is located between two intense vortices (with a high rotation rate, $Q > 0$, corresponding to $\underline{\underline{w}} > \underline{\underline{s}}$ in Figure 11). Each pair of intense vortices between two clefts forms the basis of a lobe structure, similar to an elongated tooth. Note that the spatial organisation of the lobe-and-cleft structures can be far more complex when the Reynolds number is increased as

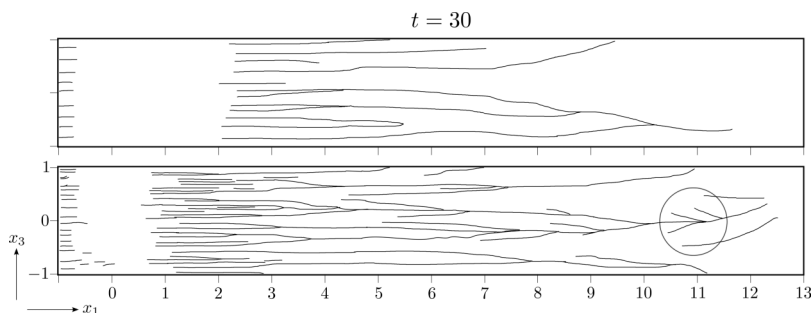


FIG. 10. Visualization in the (x_1, x_3) plane of the signature of the lobe-and-cleft structures for $t = 30$ for the simulation with $Re = 2236$ and $u_s = 0.02$ (top) and with $Re = 10\,000$ and $u_s = 0.02$ (bottom). The black circle shows an example of a fish bone skeleton instability.

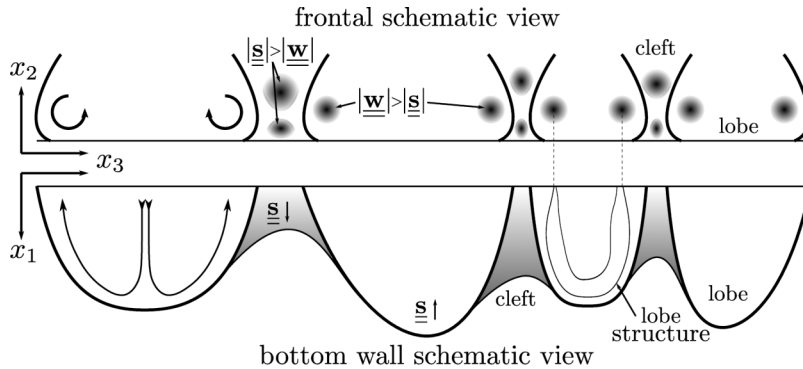


FIG. 11. Schematic representation of the lobe-and-cleft patterns.

the head of the current is more complex with a wider range of vortices and the occurrence of a new instability. The streamlines within a lobe which can be seen at the bottom left of Figure 11 can be explained by the high speed velocity inside the lobe by comparison to a lower velocity for the cleft.

The deposit map can also be examined at $t = 8$ and $t = 14$ (see Figure 12) where the longitudinal lines correspond to the signature of the clefts. It is clear that the deposition mechanism occurring at the bottom of the current is not affecting the signature of the lobe-and-cleft patterns. The signature of the structures at the head of the current is persistent for a very long time and may strongly influence the deposition mechanism. The deposition map can therefore be seen as a footprint of the front structures and can be used to better understand the lobe-and-cleft patterns. The evolution of the lobe-and-cleft patterns can be recorded in time and reproduced in space via the 2D deposition map at the wall. In particular, the merging of the lobe-and-cleft, highlighted in Figure 9, can clearly be identified especially when the head of the current is transitioning from a relatively quiet state to a more turbulent state. It is however important to note that in the present work, the

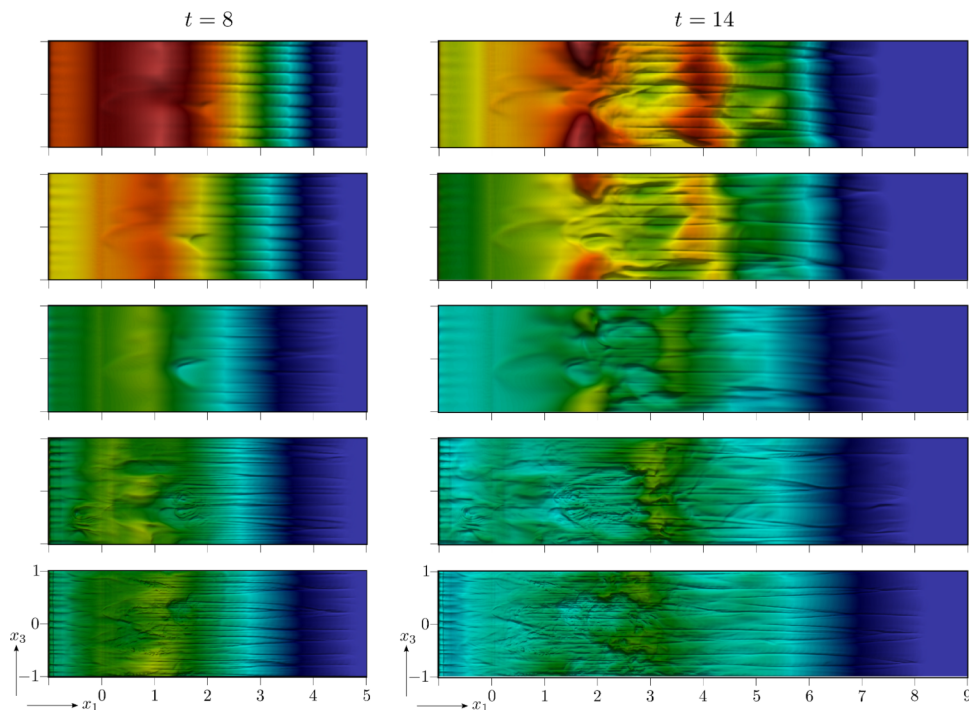


FIG. 12. Deposit map at $t = 8$ (left) and $t = 14$ (right) where the red color corresponds to the maximum deposition. Each time is scaled with its maximum. From top to bottom: $Re = 2236$ with $u_s = 0.04, 0.03, 0.02$; $Re = 5000$ and 10000 with $u_s = 0.02$.

deformation of the solid surface by either the lobe-and-cleft patterns or the deposition mechanism is not taken into account. This deformation of the solid surface could also in return affect the evolution of the lobe-and-cleft patterns and impair the deposition mechanism.

Figures 12 and 8 can be used by the geoscientist to understand the link between the deposition map and the lobe-and-cleft patterns. In particular, it can be seen that the deposition is not uniform in the spanwise direction, especially when the Reynolds number is increased. We can also see that the deposition has a wavy behavior in the streamwise direction, with two clear peaks for $Re = 10\,000$ for $x_1 \approx 2, 4$ and three peaks for $Re = 5\,000$ for $x_1 \approx 2, 4, 5$ in the streamwise direction. These figures also suggest that there might be a dependence with the size of the computational domain in the streamwise direction, highlighted by the spanwise shape of those peaks.

VII. CONCLUSIONS

Highly resolved direct numerical simulations have been presented in this paper to investigate the evolution of a mono-disperse dilute suspension particle-laden flow in the lock-exchange configuration for a channel flow. The global energy balance at different stages of the evolution of the gravity current is showing that when the settling velocity is reduced, the micro-dissipation (related to the suspended particles) is also reduced whereas the macro-dissipation (related to the turbulence) is increased. At the end of the simulations, the micro-dissipation is reduced by almost a factor 2 between the simulation with a settling velocity equal to 0.04 and the one with a settling velocity equal to 0.02. This can be explained by the fact that when the diameter of the particles is increased, the turbulence activity is reduced, with a more important drag around the particles. The settling velocity is affecting the size of the streamwise vortices at the front. The structures have a reduced size both in the spanwise and streamwise directions when the deposition is taken into account by comparison to the reference simulation with no deposition. When the Reynolds number is increased, the lobes are merging more often and earlier. A new instability has been identified only for the highest Reynolds number simulation, highlighted by fish bone skeleton structures when looking at the signature of the lobe-and-cleft structures at the front. The lobes reach a critical dimension, leading to the development of small new clefts. However, this instability is not strong enough to provoke a complete break-up of a lobe. Finally, the temporal imprint of the lobe-and-cleft structures can be recovered from the deposition map which gives very valuable information about the structures at the front of the current. The deposit map is a fingerprint of the turbulent structures at the front of the current and neither the body nor the tail of the current are able to modify it, at least under the conditions of our simulations.

As already mentioned, the next step is to carry out simulations with a larger computational domain in the spanwise direction with higher Reynolds numbers to investigate the new local instability discovered in the present simulations with $Re = 10\,000$. DNS may be too expensive in terms of computational resources for such simulations. Therefore, we are interested in using a technique developed by Ref. 36 based on high-order numerical dissipation to take into account the dissipation of the unresolved small scales, in a context of implicit large eddy simulations. Validations for this technique with the simulations presented in this paper are currently in progress and comparisons will also be carried out with the experimental data of Ref. 37, if possible.

Another direction of research would be to investigate gravity currents with a more complex bottom floor.^{23,24,38} A customized Immersed Boundary Method (IBM) can be combined with our high-order flow solver in order to model accurately 3D obstacles at the bottom of the computational domain.³⁹ The idea is to mimic the complex topographies observed in nature for turbidity currents and to see how the gravity currents are reacting to a specific topography. Finally, our customized IBM method could also be used to take into account the erosion.

ACKNOWLEDGMENTS

Present simulations have been carried out at the Pontifícia Universidade Católica do Rio Grande do Sul (PUCRS) High Performance Computing facility LAD. The authors are grateful to Petrobras for supporting this research.

- ¹ E. Meiburg and B. Kneller, "Turbidity currents and their deposits," *Annu. Rev. Fluid Mech.* **42**, 135 (2009).
- ² B. Kneller and W. McCaffrey, "Depositional effects of flow nonuniformity and stratification within turbidity currents approaching a bounding slope: Deflection, reflection, and facies variation," *J. Sediment. Res.* **69**(5), 980 (1999).
- ³ R. Britter and J. Simpson, "Experiments on the dynamics of a gravity current head," *J. Fluid Mech.* **88**, 223 (1978).
- ⁴ T. Nakajima and M. Satoh, "The formation of large mudwaves by turbidity currents on the levees of the Toyama deep-sea channel, Japan Sea," *Sedimentology* **48**(2), 435 (2001).
- ⁵ R. Wynn and D. Stow, "Classification and characterisation of deep-water sediment waves," *Mar. Geol.* **192**(1), 7 (2002).
- ⁶ N. Izumi, "The formation of submarine gullies by turbidity currents," *J. Geophys. Res.: Oceans* **109**(c3), 1–13 doi:10.1029/2003JC001898 (2004).
- ⁷ J. Simpson, *Gravity Currents in the Environment and in the Laboratory* (Cambridge University Press, 1999).
- ⁸ H. H. E. Huppert, "Gravity currents: A personal perspective," *J. Fluid Mech.* **554**, 299 (2006).
- ⁹ J. Syvitski, C. Alexander, M. Field, J. Gardner, D. Orange, and J. Yun, "Continental-slope sedimentation: The view from northern California," *Oceanography* **9**, 163 (1996).
- ¹⁰ A. Zakeri, K. Hoeg, and F. Nadim, "Submarine debris flow impact on pipelines part I: Experimental investigation," *Coastal Eng.* **55**(12), 1209 (2008).
- ¹¹ E. Nisbet and D. Piper, "Giant submarine landslides," *Nature* **392**, 329 (1998).
- ¹² J. Simpson, "Effects of the lower boundary on the head of a gravity current," *J. Fluid Mech.* **53**(4), 759 (1972).
- ¹³ M. Hallworth, H. Huppert, J. Phillips, and R. Sparks, "Entrainment into two-dimensional and axisymmetric turbulent gravity currents," *J. Fluid Mech.* **308**, 289 (1996).
- ¹⁴ J. McElwaine and M. Patterson, *XXI International Congress of Theoretical and Applied Mechanics* (Springer Verlag, Warsaw, 2004).
- ¹⁵ A. Jackson, B. Turnbull, and R. Munro, "Scaling for lobe and cleft patterns in particle-laden gravity currents," *Nonlinear Processes Geophys.* **20**, 121 (2013).
- ¹⁶ R. Bonnecaze, H. Huppert, and J. Lister, "Particle-driven gravity currents," *J. Fluid Mech.* **250**, 339 (1993).
- ¹⁷ M. Hallworth, A. Hogg, and H. Huppert, "Effects of external flow on compositional and particle gravity currents," *J. Fluid Mech.* **359**, 109 (1998).
- ¹⁸ C. Härtel, E. Meiburg, and F. Necker, "Analysis and direct numerical simulation of the flow at a gravity-current head. Part 1. Flow topology and front speed for slip and no-slip boundaries," *J. Fluid Mech.* **418**, 189 (2000).
- ¹⁹ C. Härtel, F. Carlsson, and M. Thunblom, "Analysis and direct numerical simulation of the flow at a gravity-current head. Part 2. The lobe-and-cleft instability," *J. Fluid Mech.* **418**, 213 (2000).
- ²⁰ F. Necker, C. Härtel, L. Kleiser, and E. Meiburg, "High-resolution simulations of particle-driven gravity currents," *Int. J. Multiphase Flow* **28**, 279 (2002).
- ²¹ F. Necker, C. Härtel, L. Kleiser, and E. Meiburg, "Mixing and dissipation in particle-driven gravity currents," *J. Fluid Mech.* **545**, 339 (2005).
- ²² L. Espath, L. Pinto, S. Laizet, and J. Silvestrini, "Two- and three-dimensional direct numerical simulation of particle-laden gravity currents," *Comput. Geosci.* **63**, 9 (2014).
- ²³ M. Nasr-Azadani and E. Meiburg, "Turbidity currents interacting with three-dimensional seafloor topography," *J. Fluid Mech.* **745**, 409 (2014).
- ²⁴ M. Nasr-Azadani and E. Meiburg, "Influence of seafloor topography on the depositional behavior of bi-disperse turbidity currents: A three-dimensional, depth-resolved numerical investigation," *Environ. Fluid Mech.* **14**(2), 319 (2014).
- ²⁵ M. Cantero, J. Lee, S. Balachandar, and M. Garcia, "On the front velocity of gravity currents," *J. Fluid Mech.* **586**, 1 (2007).
- ²⁶ M. Cantero, S. Balachandar, M. Garcia, and D. Bock, "Turbulent structures in planar gravity currents and their influence on the flow dynamics," *J. Geophys. Res.* **113**(C8), 1–22, doi:10.1029/2007jc004645 (2008).
- ²⁷ S. Ooi, G. Constantinescu, and L. Weber, "Numerical simulations of lock-exchange compositional gravity current," *J. Fluid Mech.* **635**, 361 (2009).
- ²⁸ W. W. E. Dietrich, "Settling velocity of natural particles," *Water Resour. Res.* **18**(6), 1615, doi:10.1029/WR018i006p01615 (1982).
- ²⁹ P. Julien, *Erosion and Sedimentation* (Cambridge University Press, 2010).
- ³⁰ M. Maxey and J. Riley, "Equation of motion for a small rigid sphere in a nonuniform flow," *Phys. Fluids* **26**(4), 883 (1983).
- ³¹ B. Lazaro and J. Lasheras, "Particle dispersion in a turbulent, plane, free shear layer," *Phys. Fluids* **1**(6), 1035 (1989).
- ³² S. K. Lele, "Compact finite difference schemes with spectral-like resolution," *J. Comput. Phys.* **103**, 16 (1992).
- ³³ S. Laizet and E. Lamballais, "High-order compact schemes for incompressible flows: A simple and efficient method with the quasi-spectral accuracy," *J. Comput. Phys.* **228**, 5989 (2009).
- ³⁴ S. Laizet and N. Li, "Incompact3d: A powerful tool to tackle turbulence problems with up to $O(10^5)$ computational cores," *Int. J. Numer. Methods Fluids* **67**, 1735 (2011).
- ³⁵ F. de Rooij and S. Dalziel, "Time- and space-resolved measurements of deposition under turbidity currents," *Spec. Pubs. Int. Ass. Sediment.* **31**, 207 (2001).
- ³⁶ E. Lamballais, V. Fortune, and S. Laizet, "Straightforward high-order numerical dissipation via the viscous term for direct and large eddy simulation," *J. Comput. Phys.* **230**(9), 3270 (2011).
- ³⁷ J. Xu, M. Noble, and L. Rosenfeld, "In-situ measurements of velocity structure within turbidity currents," *Geophys. Res. Lett.* **31**(9), L09311, doi:10.1029/2004gl019718 (2004).
- ³⁸ T. Tokyay, G. Constantinescu, and E. Meiburg, "Tail structure and bed friction velocity distribution of gravity currents propagating over an array of obstacles," *J. Fluid Mech.* **694**, 252 (2012).
- ³⁹ R. Gautier, S. Laizet, and E. Lamballais, "A DNS study of jet control with microjets using an immersed boundary method," *Int. J. Comput. Fluid Dyn.* **28**(6–10), 393 (2014).